

# Electrical Double-Layer Structure at the Rutile–Water Interface as Observed *in Situ* with Small-Period X-Ray Standing Waves<sup>1</sup>

P. Fenter,<sup>\*,2</sup> L. Cheng,<sup>\*,†</sup> S. Rihs,<sup>\*</sup> M. Machesky,<sup>‡</sup> M. J. Bedzyk,<sup>\*,†</sup> and N. C. Sturchio<sup>\*</sup>

<sup>\*</sup>Argonne National Laboratory, Argonne, Illinois 60439-4843; <sup>†</sup>Department of Materials Science and Engineering and Institute of Environmental Catalysis, Northwestern University, Evanston, Illinois 60208; and <sup>‡</sup>Illinois State Water Survey, 2204 Griffith Drive, Champaign, Illinois 61820-7495

Received August 25, 1999; accepted January 31, 2000

**X-Ray standing wave (XSW) measurements were made of Rb and Sr adsorbed from aqueous solutions at the rutile (110)–water interface. These experiments were performed to address the extent to which direct measurements of electrical double-layer structure are possible. The experimental results show that the Bragg XSW technique, using small-period standing waves generated by Bragg diffraction from the substrate, can precisely measure ion locations within the condensed layer and the *in situ* partitioning of ions between the condensed and diffuse layers. Differences in condensed layer ion positions were observed for Sr ions (measured *in situ*) as compared with Rb ions (*in situ*) and also for Sr ions (*ex situ*). An additional constraint on the *ex situ* Sr site geometry was provided by polarization-dependent surface EXAFS measurements. Such measurements can provide important constraints for the development and verification of electrical double-layer theory especially as applied to ion adsorption at the solid–water interface.**

© 2000 Academic Press

**Key Words:** electrical double layer; X-ray standing waves; mineral–fluid interface; rutile; Sr<sup>2+</sup> and Rb<sup>+</sup> adsorption.

## INTRODUCTION

Understanding the development of mineral surface charge, and the associated distribution of solute ions at solid–water interfaces, is fundamentally important for a diverse range of natural and industrial processes. Examples include environmental interfaces (1), water purification, colloidal suspensions, and the nucleation of ceramic thin films using hydrothermal processing (2). The distribution of ionic species across charged solid–water interfaces, generally referred to as the electrical double layer (EDL), has led to the development of various physical and chemical models which use mass and charge balance constraints to

explain and predict the properties of these systems (3, 4). However, relatively little is directly known about the molecular-scale structure of the EDL at the mineral–aqueous solution interface. The conventional portrait of EDL structure is shown schematically in Fig. 1a in which surface excesses and deficits of aqueous solute ions, distributed between the so-called condensed (or “Stern”) and diffuse (or “Gouy–Chapman”) layers, balance a fixed charge of a mineral surface. Figure 1 highlights one of the most basic features of the EDL, which is the partitioning of ions between the condensed and diffuse layers that is expected to be sensitive to the strength and nature of the ion–substrate interactions.

In most cases our understanding of the EDL has been hindered by a lack of quantitative molecular-scale experimental data that can be used to independently test available EDL models (1, 5). Stern-based surface complexation models use one or more capacitance values to account for the electrostatic effects associated with ion binding by mineral surfaces, and these capacitance values are typically treated as variable fitting parameters by those modeling ion adsorption data (5, 6). The microscopic significance and interpretation of these parameters are often in question. A more accurate molecular-scale picture may be afforded by the multisite surface complexation models incorporating Pauling bond-valence principles [e.g., Ref. (7)], yet such models also suffer from lack of direct structural confirmation. Thus, a precise measurement of the condensed layer ion location with respect to the underlying mineral surface lattice would be of great value in providing insight into the applicability of these models and significance of the derived parameters. However, measuring the distribution of ions within the EDL is a particularly challenging task. In addition to the normal difficulty of probing molecular-scale structures at the solid–liquid interface, there is the challenge of unraveling the relationship between the localized and delocalized ion distributions corresponding to the condensed and diffuse layers, respectively.

X-Ray techniques promise a means to elucidate the structure and composition of the EDL. The weakly interacting nature of hard X-rays enables them to probe, *in situ*, the solid–liquid interface structure. The measurements are truly quantitative, because the interaction of X-rays with matter is well understood at a

<sup>1</sup> This article has been created by the University of Chicago as operator of Argonne National Laboratory under Contract W-31-109-ENG-38 with the U.S. Department of Energy. The U.S. government’s right to retain a nonexclusive royalty-free license in and to the copyright covering this paper, for governmental purposes, is acknowledged.

<sup>2</sup> To whom correspondence should be addressed at Argonne National Laboratory, ER-203, 9700 South Cass Avenue, Argonne, IL 60439-4843. E-mail: Fenter@anl.gov.

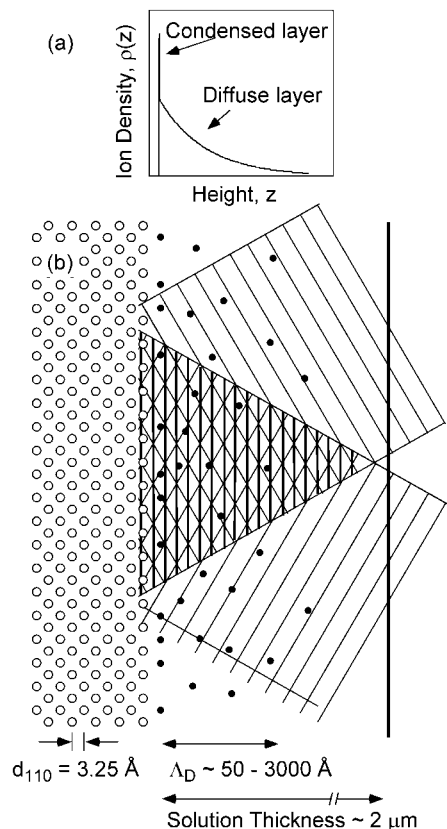


**FIG. 1.** (a) Schematic structure of the electrical double layer, showing the condensed layer and the diffuse ion distribution (characterized by the Debye length,  $\Lambda_D$ ). (b) Schematic of the XSW field, as created by the superposition of the incident and Bragg-reflected X-ray beams, and the rutile (110) substrate. Solution ions are shown as filled circles. Note that the XSW period is much smaller than the decay length of the diffuse layer.

fundamental level. X-Ray scattering techniques also naturally probe over the length scales (from  $\sim 1$  to  $\sim 10^4$  Å) normally present in an EDL. Surface X-ray diffraction and X-ray absorption spectroscopy have been used to characterize the structure of condensed layers at the electrified metal–aqueous interface (8, 9). X-Ray diffraction measurements typically provide the periodic arrangement of ions at the solid–liquid interface while X-ray absorption studies provide information about the short-ranged order near the element of interest (10, 11). Other “direct” studies of the condensed layer structure in systems more relevant to natural systems (e.g., near colloids or mineral–fluid interfaces) typically view the condensed layer as “slab” specified by a thickness and density, and consequently have not yet achieved a truly atomistic view of the EDL structure (12, 13). The long-period X-ray standing wave technique has been used to directly probe the Debye length associated with the diffuse layer (14).

Here we demonstrate the use of the Bragg X-ray standing wave (XSW) technique with a high-brilliance synchrotron to probe the ion distribution near a mineral–fluid interface. In particular, we show that this XSW technique measures: (1) the precise location of ions in the condensed layer and (2) the par-

titution of ions between the condensed and diffuse layers of the EDL. We demonstrate this capability by investigating the behavior of alkali and alkaline-earth ions ( $\text{Rb}^+$  and  $\text{Sr}^{2+}$ ) at the rutile (110)–water interface over a range of pH values and ion concentrations. The results show significant differences in the behavior of  $\text{Rb}^+$  and  $\text{Sr}^{2+}$  ions and reveal differences in the condensed layer structure of  $\text{Sr}^{2+}$  ions between *in situ* and *ex situ* conditions. In addition, we present *ex situ* surface extended X-ray absorption fine-structure (SEXAFS) spectroscopy measurements for Sr that complement the XSW measurements by providing an additional constraint on the Sr site geometry in the condensed layer. Definitions of symbols and abbreviations used in this article are listed in the Appendix.

## MATERIALS AND METHODS

We used the (110) surface of the  $\text{TiO}_2$  polymorph rutile for this study because it has been studied extensively and is known to be chemically stable over a broad range of pH values (15). The structure of the rutile (110) surface has been measured (16) under ultrahigh-vacuum conditions and found to exhibit only minor structural relaxations in the near-surface region. The (110) and (100) surfaces are thought to be the predominant faces on most powdered rutile specimens used in potentiometric titration investigations of ion adsorption and related phenomena (17–19), and the types and distribution of surface groups on the (110) and (100) faces are similar (20, 21). The behavior of the (110) surface should therefore be representative of many powdered rutile specimens. This hypothesis is supported by the similarity of the points of zero charge pH ( $\text{pH}_{\text{zpc}}$ ) of these systems [ $\text{pH}_{\text{zpc}} \sim 5.6$ – $5.7$  for the rutile (110) surface (22, 23), which is similar to the measured  $\text{pH}_{\text{zpc}}$  of about 5.4–6 for powdered rutile specimens (6, 17, 24, 25)].

### Sample Preparation

Chemomechanically polished synthetic single-crystal rutile (110) substrates (Princeton Scientific Corp., Princeton, NJ) were cleaned ultrasonically in methanol to remove any surface organic contamination. Three ultrasonic baths in nanopure ( $\sim 18$  MΩ/cm) deionized water followed. Experimental solutions were prepared by dissolving reagent-grade  $\text{RbCl}$ ,  $\text{RbOH}$ , or  $\text{Sr}(\text{NO}_3)_2$  in nanopure deionized water. Solution pH values, adjusted by using  $\text{HNO}_3$  and/or  $\text{NaOH}$ , ranged from 2.98 to 10.92. The total aqueous concentrations of Rb and Sr in the experimental solutions,  $[\text{Rb}]_{\text{aq}}$  and  $[\text{Sr}]_{\text{aq}}$ , ranged from 0.9 to 1280  $\mu\text{M}$ , and were measured by using inductively coupled plasma atomic emission spectrometry (for  $[\text{Sr}]_{\text{aq}}$ ) and inductively coupled plasma mass spectrometry (for  $[\text{Rb}]_{\text{aq}}$ ). Solution ionic strengths,  $I$ , ranged from 590 to 4240  $\mu\text{M}$ . Solution compositions are listed in Table 1. The aqueous speciation of Rb and Sr in the solutions was calculated by using the Geochemist’s Workbench code (26);  $[\text{Rb}]_{\text{aq}}$  was exclusively present as  $\text{Rb}^+$  in all solutions, and  $\geq 98.5\%$  of  $[\text{Sr}]_{\text{aq}}$  was present as  $\text{Sr}^{2+}$ .

**TABLE 1**  
**Chemical Analyses and Derived Ionic Strengths**  
**of Solutions ( $\mu\text{M}$ )<sup>a</sup>**

pH	Na	Rb	Sr	NO <sub>3</sub> <sup>b</sup>	Cl <sup>b</sup>	I	<i>In situ</i>	<i>Ex situ</i>
3.20	0	0	1280	2690	0	4240		✓ <sup>a</sup>
7.90	0	1240	0	0	1240	1240	✓	
9.89	0	610	0	0	610	610	✓	
10.64	810	0	140	280	0	1050	✓	
10.70	660	0	000.9	1.8	0	590		✓
10.74	660	0	11	23.	0	650	✓	✓
10.70	660 <sup>b</sup>	0	1280	2560	0	3150		✓
10.92	1000	4.8	12	24	4.8	1040	✓	

<sup>a</sup> The check marks in the last two columns identify the solutions used for *in situ* and *ex situ* experiments.

<sup>b</sup> Calculated from stoichiometry of reagents.

The sample was held in a Kel-F “thin-film” cell using an 8- $\mu\text{m}$ -thick Kapton film as an X-ray window, in which a thin solution layer is held against the sample surface through capillary action. For the *in situ* measurements, the experimental solution was manually injected into the cell in such a way as to expand the solution layer confined by the Kapton film to a thickness of about 1 mm. This solution layer was allowed to react with the sample surface for 6 min prior to minimizing the thickness of the solution layer. A pump was then used to apply a negative pressure to reduce and maintain the thickness of the solution layer to  $\sim 2 \mu\text{m}$  (14) using the system shown schematically in Fig. 2. The mechanical pump was connected to a 60-cm<sup>3</sup> syringe (piston end) with wide-bore Tygon tubing, and the syringe (outlet end) was connected to the sample cell through a polyvinyl chloride tubing (inner diameter = 1.65 mm) with luer-lock fittings. Between *in situ* measurements, the sample surface was cleaned by exposure to 1000  $\mu\text{M}$  nitric acid solution following

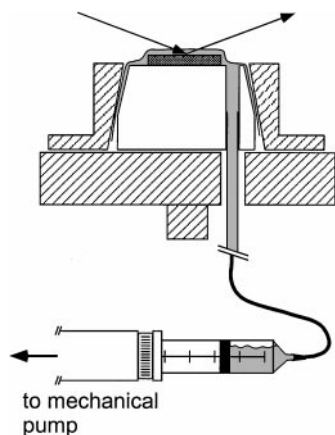


**FIG. 2.** Schematic drawing of the thin-film cell geometry used in this study. The rutile sample was held under a thin Kapton film on a Kel-F block, in which the solution thickness was minimized by applying a negative pressure to the solution through the syringe. The cell body (hatched area) was made of aluminum.

the same procedure. Using X-ray fluorescence measurements we confirmed that this procedure produced a clean rutile surface that was free of any adsorbed Sr or Rb ion with a sensitivity limit of  $\sim 5 \times 10^{-4}$  ions/ $\text{\AA}^2$ . For the *ex situ* measurements, the sample surface was covered with a mound of experimental solution (several drops) and allowed to react for 6 min. The sample was then tilted so that the solution dropped off (onto absorbent paper), and the surface was then enclosed in a polyethylene balloon filled with flowing high-purity He gas for the duration of the XSW measurement. Care was taken to ensure that no residual droplets of experimental solution adhered to the sample in the region illuminated by the X-ray beam. The sample surface was cleaned between *ex situ* measurements by reacting it with 1000  $\mu\text{M}$  nitric acid solution in the same manner.

### The XSW Technique

The Bragg diffraction XSW technique has been described previously (27). Briefly, an XSW field is generated by a coherent superposition of the incident and reflected X-ray beams during Bragg diffraction (28). The XSW period is equal to the  $d$  spacing of the diffraction planes, and the position of the XSW antinodes shifts inward by  $d/2$  relative to the diffraction planes as the incident angle,  $\theta$ , is scanned through the Bragg reflection (see Fig. 1b). The atomic position and distribution (characterized by the coherent position and coherent fraction, respectively) are determined by monitoring the modulation of the fluorescence yield of a specific atomic species near the Bragg condition. The fluorescence yield, normalized to the off-Bragg yield, varies as

$$Y(\theta) = 1 + R(\theta) + 2[R(\theta)]^{1/2} f_H \cos[\phi(\theta) - 2\pi P_H], \quad [1]$$

where the reflectivity  $R(\theta)$  and the XSW phase  $\phi(\theta)$  are derived for the  $H = (hkl)$  diffraction condition from dynamical diffraction theory. Each set of XSW data is fully characterized by two model-independent parameters: the coherent position,  $P_H$ , and the coherent fraction,  $f_H$ . The parameters  $f_H$  and  $P_H$  are obtained from a  $\chi^2$  fit of Eq. [1] to the XSW data. Uncertainties in  $f_H$  and  $P_H$  are typically smaller than  $\pm 0.03$ , on the basis of counting statistics and a sensitivity analysis of the fitting procedure. In this study,  $H$  corresponds to the rutile (110) Bragg diffraction condition, and thus we denote  $f_{110}$  and  $P_{110}$  simply as  $f$  and  $P$ .

To assign the physical significance of these two parameters to the EDL we must first define the “condensed” and “diffuse” layers with regard to the XSW measurements. We take as an operational definition that the condensed layer consists of ions whose locations are essentially fixed at the mineral–water interface but which may be freely exchanged with the solution. This definition of the condensed layer does not explicitly differentiate between “inner-sphere” and “outer-sphere” surface complexes. Provided each complex has a well-defined location with respect to the substrate lattice, a distinction between these two complexes would be found primarily in their respective ion locations and the nature of their ion–substrate interactions.

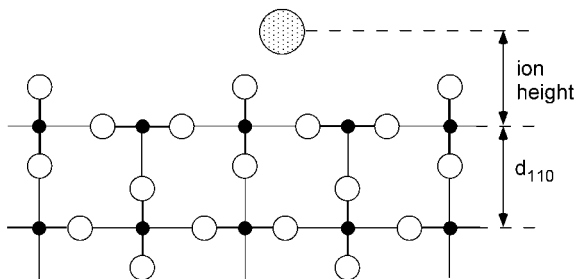


**FIG. 3.** Schematic perspective view of an unrelaxed rutile (110) surface (titanium and oxygen atoms are shown as small filled and large open circles, respectively). Also shown schematically is the ion height that is measured by XSW with respect to the unrelaxed surface plane.

Similarly, we assume that any ions present in excess (relative to their bulk solution concentrations) near the mineral–water interface as a result of the mineral surface charge and that do not have a well-defined position are in the diffuse layer.

Within these definitions, the coherent position  $P$  is the position of the condensed layer ions measured with respect to the unrelaxed rutile surface lattice as shown in Fig. 3. The coherent position is normalized to the  $d$  spacing of the Bragg plane used to create the X-ray standing wave [in the case of the rutile (110) reflection,  $d_{110} = 3.25 \text{ \AA}$ ] and consequently  $P = 0$  or  $1$  corresponds to ions that are located in a projected (110) diffraction plane. The coherent fraction  $f$  is essentially the fraction of the fluorescence-selected ions that resides in the condensed layer. These assignments are justified in more detail below.

The XSW technique relies on measuring the X-ray fluorescent radiation from the ion of interest. It is applicable (in the configuration used here) to study ions whose X-ray fluorescent lines are attenuated by less than  $\sim 90\%$ , through the  $\sim 10\text{-}\mu\text{m}$ -thick layer consisting of the  $2\text{-}\mu\text{m}$  solution layer and  $8\text{-}\mu\text{m}$  Kapton film, at a typical takeoff angle with respect to the surface plane of  $\sim 2^\circ$ . This restricts the application to X-ray fluorescent emission energies above  $\sim 5 \text{ keV}$ , which are characteristic of elements having  $Z > 23$  ( $K$ -edge emissions) and  $Z > 57$  ( $L$ -edge emissions). In this study, we use Rb and Sr as representative alkali- and alkaline-earth metals, respectively. The XSW results for Rb and Sr can be compared with those of recent potentiometric titration studies of Na and Ca on rutile powders (6, 15, 18, 19).

#### Experimental Details of the XSW Measurement

The XSW measurements were performed at the 12-ID-D undulator beamline of the BESSRC sector at the Advanced Photon Source located at Argonne National Laboratory. It is the need for a high-flux X-ray beam with negligible divergence and a small cross section (i.e., high brightness) that necessitates the use of the Advanced Photon Source (APS) for these studies. A monochromatic X-ray beam was obtained using a double-bounce Si(111) monochromator resulting in a nominal energy width of  $\Delta E/E = 1.4 \times 10^{-4}$  (29). The photon energies were chosen to be 16.7 and 16.2 keV for the  $\text{Sr}^{2+}$  and  $\text{Rb}^+$  measure-

ments, respectively, with corresponding  $\text{TiO}_2(110)$  Bragg angles of  $6.77^\circ$  and  $6.56^\circ$ . The  $\text{Sr}K\alpha$  and  $\text{Rb}K\alpha$  fluorescence emission lines at 14.2 and 13.4 keV were monitored using a Si(Li) solid-state detector having an energy resolution of 270 eV at 13 keV, and the Bragg reflectivity was measured using an ion chamber. No measurable background Sr or Rb fluorescence was observed from the clean rutile substrate crystal, Kel-F cell, Kapton film, or polyethylene used in the experiments.

XSW analysis of surface adsorption in the Bragg geometry usually requires a near-perfect single-crystal substrate. The rutile (110) substrate was observed to have a strong mosaic texture exhibiting a full-width at half-maximum (FWHM) of  $\sim 0.015^\circ$  for the (110) reflection. This is much larger than the FWHM of  $0.0018^\circ$  that is predicted by dynamical diffraction theory for a perfect rutile single crystal. By using a beam that had a cross section of  $0.02 \text{ mm}$  vertical  $\times 0.2 \text{ mm}$  horizontal (resulting in a beam footprint of  $0.17 \text{ mm} \times 0.20 \text{ mm}$ ) and carefully searching across the crystal surface, we found regions where the rocking curve width was only 15–30% broader than theoretical [after taking into account the additional broadening due to the dispersion of the Si(111) monochromator]. In this configuration the X-ray beam flux was  $\sim 2 \times 10^9$  photons per second. The rutile crystal was found to have a  $0.32^\circ$  surface miscut with respect to the (110) crystalline planes. The direction of the miscut was oriented in the direction perpendicular to the scattering plane for these measurements.

We model the finite mosaic broadening by incoherently averaging the reflectivity curves and XSW yields from a collection of “perfect single-crystal” grains having a small mosaic spread of  $\leq 8 \mu\text{rad}$ . This method provides a simple phenomenological way of explaining the broadening, and allows us to quantify the changes in EDL structure and ion partitioning in this system. Because of the associated uncertainties, we do not consider the coherent position to be reliably measured for  $f < 0.15$ .

#### Experimental Details of the SEXAFS Measurements

Polarization-dependent Sr  $K$ -edge SEXAFS (30) measurements were performed at beamline X15A of the National Synchrotron Light Source under *ex situ* conditions. XSW measurements confirmed that it exhibited a Sr adsorption structure similar to that previously studied with XSW at the APS. The SEXAFS measurements were made with the polarized X-rays, with the  $E$ -field parallel to the in-plane [001] and  $[-110]$  directions and the normal [110] direction, respectively. In each case the X-ray beam was incident on the sample surface at a low angle ( $7^\circ$ – $8^\circ$ ). The crystallographic orientation of the in-plane directions was determined with a transmission Laue image taken with a white synchrotron beam. The X rays were monochromated by a double-crystal Ge(111) monochromator and the photon energy was scanned through the Sr  $K$  absorption edge. The energy range was 16.040–16.600 keV for the in-plane scans and 16.050–16.300 keV for the normal scan using 1-eV steps. Data were collected in fluorescence mode on the  $\text{Sr}K\alpha$  emission with a Si(Li) solid-state detector. Equivalent data were taken for an

experimental standard of SrO crystalline powder in transmission mode with a photodiode detector.

SEXAFS data analysis was performed using the MacXAFS software package (Version 4.1) (31) according to standard procedures (32, 33). The first-shell filtering was done by first Fourier-transforming the background-subtracted data into  $R$  space over the range  $k = 2.3\text{--}9.4 \text{ \AA}^{-1}$  with modified Hanning windows of 0.5 and  $1.5 \text{ \AA}^{-1}$  for the in-plane data, and over the range  $k = 2.3\text{--}7.2 \text{ \AA}^{-1}$  with windows of 0.5 and  $1.1 \text{ \AA}^{-1}$  for the normal data. The  $R$ -space data were subsequently back-transformed over the ranges  $R = 1.05\text{--}2.83 \text{ \AA}$  for the in-plane data and  $R = 0.87\text{--}2.95 \text{ \AA}$  for the normal data, with  $0.31\text{-\AA}$  windows. In each case, equivalent transform was done for the SrO standard data. This absorption data were fit in phase,  $\phi(k)$ , and amplitude,  $|f(k)|$ , with respect to that for the SrO standard, according to the equation

$$\chi(k) = N|f(k)| \sin[2kR + \phi(k)] \exp(-2k^2\sigma^2), \quad [2]$$

where the fitting parameters  $N$ ,  $R$  and  $\sigma^2$  are the first-neighbor Sr–O coordination number, radial distance, and mean square vibrational amplitude, respectively. The best-fit parameters are obtained by minimizing the difference between filtered experimental and calculated data in both its phase and amplitude. The final fit was performed with an optimized, fixed step-edge shift and an amplitude reduction factor of 0.95.

## RESULTS

### *Ex Situ Coverage Measurements of Sr Adsorption on Rutile*

We first performed a set of *ex situ* Sr coverage measurements as a function of pH and Sr solution concentration,  $[\text{Sr}]_{\text{aq}}$ . These results are summarized in Fig. 4. The observed behavior was reversible. The absolute *ex situ* Sr coverage,  $\Theta_{\text{tot}}$ , was measured

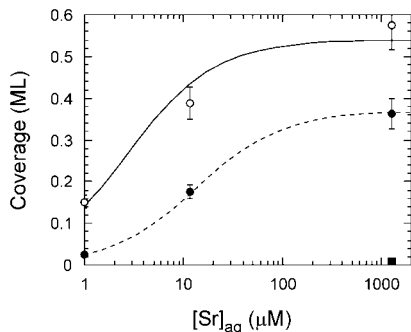


**FIG. 4.** *Ex situ* measurements of the total  $\text{Sr}^{2+}$  ion coverage adsorbed at the rutile (110) surface (after emersion) as a function of  $[\text{Sr}]_{\text{aq}}$ . Data are shown for  $\text{pH} \sim 10.7$  (open circles) and  $\text{pH} 3.2$  (filled square). Also shown is the “coherent coverage,”  $\Theta_{\text{coh}} = \Theta_{\text{tot}} f$  (filled circles), at  $\text{pH} \sim 10.7$ , where  $f$  is the measured coherent fraction of Sr at each concentration. The solid and dashed lines are a fit to the data using a Langmuir adsorption isotherm described in the text for the total and coherent coverages, respectively.

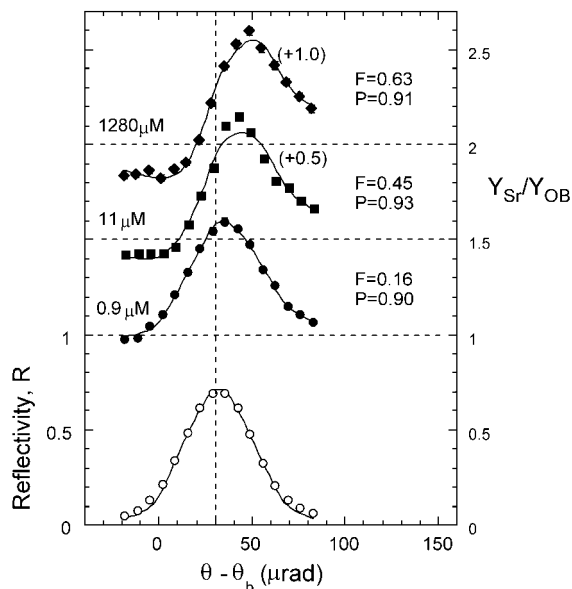


**FIG. 5.** *Ex situ* XSW results for  $\text{Sr}^{2+}$  ions adsorbed at the rutile (110) surface (after emersion) at the specified values of  $[\text{Sr}]_{\text{aq}}$ . In each case the fluorescent yield and reflectivity are plotted as function of the angle of incidence,  $\theta$ , measured with respect to the surface plane. Here  $\theta_b$  is the rutile (110) Bragg angle in the absence of refraction. Each set of XSW data is offset vertically by 0.5 for clarity, and the dashed horizontal lines indicate the asymptotic limit of the normalized off-Bragg fluorescence yield,  $Y_{\text{Sr}}/Y_{\text{OB}} = 1.0$ , for each data set. The derived XSW parameters,  $f$  and  $P$ , and solution ion concentration,  $[\text{Sr}]_{\text{aq}}$ , are shown.

using Sr fluorescence (calibrated with an As-implanted silicon wafer with a density of  $10^{15}$  As atoms/cm<sup>2</sup>). At a relatively high solution concentration,  $[\text{Sr}]_{\text{aq}} = 1280 \text{ \mu M}$ , the *ex situ* surface coverage depends strongly on the solution pH. While 0.57 monolayer (ML) Sr adsorbs at  $\text{pH} 10.7$  (open circles, Fig. 4),  $<0.01$  ML Sr is adsorbed on the rutile surface exposed at  $\text{pH} 3.2$  (filled squares, Fig. 4) [1 ML is defined as one ion per  $19.24 \text{ \AA}^2$ , corresponding to the density of bridging oxygen atoms on the rutile (110) surface]. This is a clear indication that the Sr ion coverage is controlled, at least in part, by the rutile surface charge and is consistent with the measured  $\text{pH}_{\text{zpc}}$  values for the 110 face of rutile of 5.6–5.7 (22, 23). Consequently,  $\text{Sr}^{2+}$  adsorption is expected to be negligible one or more pH units below the  $\text{pH}_{\text{zpc}}$  where the surface has an appreciable net positive charge [e.g., (17–19)]. These data also show that the *ex situ* Sr surface coverage depends strongly on the solution Sr concentration: the coverage is largest at  $\text{pH} 10.7$  when the solution Sr concentration is the largest.

### *Ex Situ XSW Results*

*Ex situ* XSW measurements as a function of Sr solution concentration are shown in Fig. 5. As expected based on Eq. [1], the Sr fluorescent yields show a clear enhancement near the peak of the  $\text{TiO}_2$  (110) Bragg reflectivity (shown as a dashed vertical line in Fig. 5). However, the angular variation of the Sr fluorescence is shifted with respect to the  $\text{TiO}_2$  reflectivity, and the normalized fluorescent yield,  $Y_{\text{Sr}}/Y_{\text{OB}}$ , is observed to be less

than 1 on the small angle side of the Bragg peak. ( $Y_{\text{Sr}}/Y_{\text{OB}} = 1$  corresponds to the fluorescent yield in the absence of a reflected X-ray beam and is noted for each data set as a dashed horizontal line.) These are unambiguous indications of the standing wave effect which correspond to the interference term proportional to  $f_H \cos[\phi(\theta) - 2\pi P_H]$  in Eq. [1].

On analyzing these data using Eq. [1], we derive the coherent position,  $P$ , and coherent fraction,  $f$ , of the Sr ions as a function of  $[\text{Sr}]_{\text{aq}}$ . We find that  $P$ , within error, remains constant at  $P = 0.91$ . However,  $f$  is found to vary significantly from 0.16 to 0.63 with  $[\text{Sr}]_{\text{aq}}$  ranging from 0.9 to 1280  $\mu\text{M}$ , such that the largest  $f$  is observed for samples exposed to the highest  $[\text{Sr}]_{\text{aq}}$ . In the simplest interpretation of these *ex situ* data,  $f$  represents the fraction of ions located in an adsorption site whose location is defined by  $P$  with the remaining ions being adsorbed at random locations on the surface (e.g., due to rapid nonequilibrium deposition during the emersion process). This implies that the highest degree of uniformity in the Sr ion location is found when the samples are exposed to the highest solution  $[\text{Sr}]_{\text{aq}}$ . If two or more adsorption sites were to coexist, the coherent position would measure the average height of those adsorption sites (weighted by the respective coverage of each site). We can then conclude either that there exists a single adsorption site over this range of conditions or, if there is more than one adsorption site, that the relative populations of these sites must be fixed. More detailed measurements will be able to distinguish between these possibilities. Consequently all subsequent references to the ion adsorption site should be understood as including both possibilities (with the height referring to the average condensed layer ion height in the case when there is more than one ion site in the condensed layer).

Combining the *ex situ* XSW results with the *ex situ* coverage measurements discussed above, we can derive the ‘‘coherent coverage’’ which we define as  $\Theta_{\text{coh}} = \Theta_{\text{tot}} f$ . The coherent coverage represents the absolute *ex situ* coverage of Sr ions located in a Sr adsorption site at each concentration, and is plotted along with the total coverage in Fig. 4 (filled circles). While the total Sr coverage is found to vary by a factor of  $\sim 4$  for  $[\text{Sr}]_{\text{aq}}$  varying from 0.9 to 1280  $\mu\text{M}$ , the coherent coverage is found to vary by a factor of  $\sim 20$  over this concentration range. This suggests that the changes in the *ex situ* coherent coverage (and, to a lesser extent, the total *ex situ* coverage) are driven by changes in the *in situ* rutile–water interface structure, and are likely to be associated with the EDL structure.

### Ex Situ SEXAFS Results

The  $k^2$ -weighted EXAFS  $\chi(k)$  functions for the raw and the Fourier-filtered first-shell data, for each of the three polarization measurements are shown in Fig. 6. The best-fit results are listed in Table 2 where the parameter  $\Delta\sigma^2$  in Table 2 represents the difference in  $\sigma^2$  relative to the SrO standard. The uncertainty in  $N$  is estimated to be  $<20\%$ , and that in  $R$  is  $\leq 0.02$   $\text{\AA}$ .

These results for Sr adsorbed at a rutile surface reveal that the Sr ion is bonded to the surface O atoms at a bond length com-

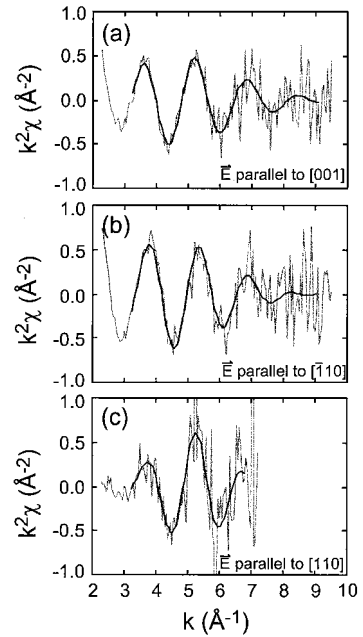


**FIG. 6.**  $k^2$ -Weighted Sr EXAFS data are shown in the form of the  $\chi(k)$  function after background removal (ragged line) and its first-shell component (smooth line). Data are shown for three orientations of the electric field vector,  $E$ , along the (a) (001), (b)  $(-110)$ , and (c) (110) crystallographic directions.

parable to that in the SrO crystal, but in a somewhat distorted octahedral coordination. The distortion is such that the octahedron is flattened in the surface normal direction and somewhat elongated in the in-plane  $[-110]$  direction. From XSW measurements performed on the same sample as the SEXAFS measurements, we infer (from the coherent fraction) that only 40–50% of the surface Sr ions are found in the site defined by the XSW measurements, as described above, with the remaining ions located in a random distribution of sites. The SEXAFS data were therefore a sampling of both the ordered and the random portions of the surface Sr species. However, the fact that the first-shell data reveal a unique bonding distance typical of a Sr–O octahedron indicates that the random portion does not affect the interpretation for the ordered fraction of the data. The outer-shell contributions in the raw data, particularly the Sr–Ti shell, are not significant, indicating that they are partially obscured by the random portion of the data and perhaps suggesting that the

**TABLE 2**  
SEXAFS Parameters as a Function of the Orientation of the Electric Field Vector Derived from the Data in Fig. 6

$E$ polarization	$N$ (effective)	$R$ ( $\text{\AA}$ )	$\Delta\sigma^2$ ( $\text{\AA}^2$ )
$[-110]$	9.42	2.58	0.008
$[001]$	7.23	2.60	0.003
$[110]$	4.8	2.62	0.003
SrO standard	6.0	2.58	

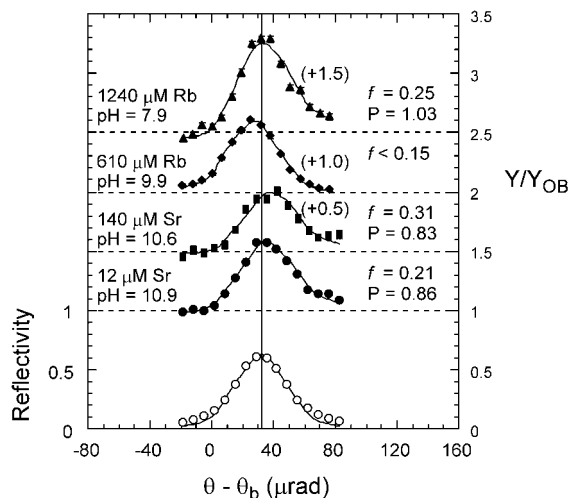


**FIG. 7.** *In situ* XSW data for Sr and Rb adsorbed at the rutile (110)–water interface at alkaline pH. The pH, bulk solution concentration, and derived XSW parameters,  $f$  and  $P$ , are shown for each measurement. Each set of XSW data is offset vertically by 0.5 for clarity (the dashed horizontal lines indicate the asymptotic limit of the normalized off-Bragg fluorescence yield of 1.0 for each data set).

Sr ion is located at a site where the Sr–Ti scattering is weak for the particular polarizations used in the measurements.

#### *In Situ* XSW Results

*In situ* XSW data for both Sr and Rb, as a function of solution concentration, are shown in Fig. 7. The modulation of the Sr fluorescence as a function of angle is much weaker in these data than in the *ex situ* data (Fig. 5). This indicates smaller  $f$  values for the *in situ* measurements. *In situ* XSW measurements of Sr adsorption with  $[\text{Sr}]_{\text{aq}} = 12 \mu\text{M}$  at pH 3.2 (not shown) reveal a negligible coherent fraction indicative of a random Sr ion location. This is expected based on the *ex situ* coverage measurements that revealed an insignificant Sr ion coverage adsorbed to the rutile surface under these conditions (see Fig. 4). This suggests that the nonzero  $f$  values derived from the *in situ* measurements at pH  $\sim 11$  reflect the *in situ* Sr adsorption structure. In the case of Sr adsorption, the *in situ*  $P$  value for Sr is  $\sim 7\%$  smaller than the *ex situ* value discussed above. The overall similarity between the *in situ* and *ex situ* results suggest that the Sr ion location is determined primarily by the ion–substrate interaction, and further supports our conclusion of a well-defined adsorption site. It also provides confidence in the derived Sr ion location for the *in situ* measurements despite the relatively small coherent fractions found in those measurements. However, the small but finite difference between these results appears to be significant especially as it is found systematically over a broad range of solution ion concentrations. This suggests that the adsorbed Sr location exhibits some sensitivity to its environment, but this result needs to be confirmed with further measurements. Also shown in Fig. 7 are the *in situ* results for the adsorption of Rb, which show behavior qualitatively similar to that of Sr,

albeit at a much higher solution concentration and somewhat different pH values. In particular, the coherent position for Rb is found to be significantly larger than that of Sr.

## DISCUSSION

### *Condensed Layer Structure*

Measurements of the condensed layer position as a function of ion species, solution concentration, and experimental conditions (*in situ* vs *ex situ*) are summarized in Fig. 8. Assuming that the adsorbed ions are located in the first lattice plane above the rutile surface, we derive ion heights,  $z = d_{110} P$ , of  $\text{Rb}^+$  and  $\text{Sr}^{2+}$  ions to be 3.35 and 2.75 Å, respectively (where  $d_{110}$  is the rutile (110) Bragg plane spacing,  $d_{110} = 3.25 \text{ Å}$ , and  $P$  is the measured coherent position). The difference in the adsorbed Rb and Sr heights (0.6 Å) is somewhat larger than the difference between their ionic radii (0.46 Å) (34). This suggests that the differences in the condensed layer structure of these ions may be due in part to differences in their ionic charges and adsorption geometries (e.g., mono-, bi-, or tetradentate adsorption geometries).

The measured height of  $\text{Sr}^{2+}$  ions is larger *ex situ* by 0.2 Å than *in situ*. This does not necessitate a change in the surface oxygen–cation bond length because these bonds in principle are free to rotate, and the XSW data only constrain the ion height. Nevertheless, the magnitude of this change is sufficiently large to suggest that high-resolution structural data (i.e., with a precision of  $\sim 0.05 \text{ Å}$ ) taken in the absence of an aqueous solution may not reflect the precise *in situ* structure of the EDL. For comparison, a previous study of Pb ions adsorbed on the calcite (104) surface showed no measurable differences between *in situ* and *ex situ* measurements (35). This result suggests that the influence of the solution is weaker for the case of ions incorporated into the outermost layer of the substrate lattice (as is the case in Pb/calcite) as compared with the case where the ion is adsorbed on top of the substrate surface (as we believe is the case for  $\text{Sr}^{2+}$  on rutile).

By combining the *in situ* and *ex situ* XSW measurements with the *ex situ* SEXAFS measurements and making use of the

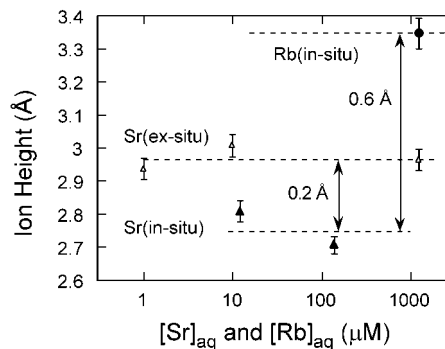


**FIG. 8.** Summary of the condensed layer ion height as a function of aqueous concentration for Sr and Rb. Also included is the change in the condensed layer ion height between *in situ* and *ex situ* measurements.

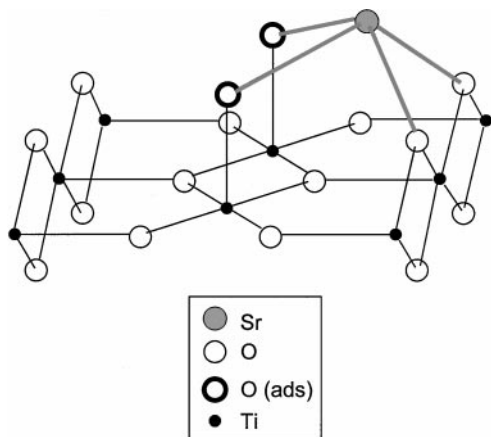


**FIG. 9.** Perspective view of the derived Sr adsorption site based on the *ex situ* and *in situ* XSW data, as well as the *ex situ* SEXAFS data. Note that the condensed layer Sr atoms interact with the rutile (110) surface through both the bridging oxygen atoms and the adsorbed oxygen species,  $O_{\text{ads}}$ .

previously published relaxation of the rutile (110) surface structure (16), we can construct a model for the adsorption of Sr to the rutile surface. Together the observed range of Sr heights of 2.75–2.95 Å (derived from the *in situ* and *ex situ* XSW data) and the observed Sr–O bond length of 2.60 Å (from the SEXAFS data) imply that the Sr ion does not interact directly with the oxygen atoms in the Ti–O surface plane. Instead, these results imply that it interacts only with the bridging oxygen atoms that are  $\sim 1$  Å above the Ti–O plane. If we start with the reasonable assumption that the divalent Sr ion bridges between the bridging oxygen atoms (e.g., bidentate bonding) this provides us with enough information to uniquely define the adsorbed Sr location (see Fig. 9). Previous studies have concluded that a substantial fraction of the nominally bare Ti atoms in the surface plane (as seen in Fig. 3) adsorb water either molecularly or dissociatively on exposure to either water vapor or aqueous solutions (10). We can generically refer to these adsorbed species (e.g., OH,  $\text{OH}_2$ , . . .), as  $O_{\text{ads}}$  species. If we place this species at a height of 1.98 Å (corresponding to the Ti–O bond length in rutile) directly above the nominally bare Ti atom (as seen in Fig. 3), we find that this  $O_{\text{ads}}$  species is also coordinated with the adsorbed Sr atom through a 2.7-Å bond length. If we do the same calculation for an unrelaxed rutile surface, we derive a Sr– $O_{\text{ads}}$  bond length of 2.4 Å. The range of calculated bond lengths easily brackets the value of 2.60 Å determined by the *ex situ* SEXAFS data. Had we assumed a monodentate bonding between the Sr ion and the bridging oxygen atoms, this would imply a Sr– $O_{\text{ads}}$  bond length of less than 1.5 Å which is chemically unreasonable. The derived model, as shown in Fig. 9, suggests that Sr adsorbs in a tetradentate configuration to two bridging oxygen atoms and two  $O_{\text{ads}}$  species.

While there is clearly some ambiguity associated with the assumptions that were made in deriving this model, further work will be able to test these assumptions and to provide an unambiguous determination of the Sr adsorption site (or sites) within

the condensed layer. However, the coupling of the SEXAFS and XSW results proves to be a powerful combination that provides a much more detailed picture of the condensed layer than would have been possible with either technique alone.

#### *Comparison of Condensed Layer Structure to Previous Potentiometric Titration Studies*

Capacitance values are derived from model fits to ion adsorption data in potentiometric titration studies (6, 18). In contrast, the present *in situ* XSW measurements directly probe the ion height. To compare the results of these two different types of experiments, we estimate the capacitance of the condensed layer using the measured Sr and Rb ion heights according to  $C = \epsilon_0 \epsilon_b / d$ , where  $C$  is the capacitance per unit area (in units of  $\text{F}/\text{m}^2$ ),  $\epsilon_0$  is the permittivity of a vacuum ( $8.854 \times 10^{-12}$ ),  $\epsilon_b$  is the bulk dielectric constant of the condensed layer, and  $d$  is the distance of charge separation (in meters). A maximum  $\epsilon_b$  value can be taken to be the bulk value for water (78.5); lower values are possible as a result of dielectric saturation effects within the condensed layer (1). If we estimate the distance of charge separation to be that of the ion above the average surface oxygen height (both bridging and adsorbed) of 1.5 Å, this results in values of  $d_{\text{Sr}} = 1.3$  Å and  $d_{\text{Rb}} = 1.9$  Å. Taking  $\epsilon_b$  equal to 78.5 results in estimated capacitance values of about 3.8  $\text{F}/\text{m}^2$  and 5.6  $\text{F}/\text{m}^2$  for Rb and Sr layers, respectively, based on the XSW measurements. In comparison, the potentiometric titration measurements reveal that the best-fit capacitance values for Na on rutile are typically near 2  $\text{F}/\text{m}^2$  (6), and a capacitance value of 2.8  $\text{F}/\text{m}^2$  was estimated for Sr with the assumption that a bidentate surface complex is formed (18). These values are  $\sim 50\%$  smaller than the capacitances derived through the XSW measurements.

Several factors should be considered in comparing the capacitance values derived through these two different techniques. First, for similar solution concentrations of a particular ion, the ratio of ion concentration to solid surface area is typically much larger (often by a factor of  $10^4$  to  $10^5$ ) in single-crystal studies than in powder studies. Consequently, the degree of surface coverage can be much greater in single-crystal studies. Second, ionic strength and pH values were not controlled as tightly in this study as they typically are in powder studies. Third, the best-fit capacitance values from model simulations typically covary with other model parameters (5, 6), such as the adsorption equilibrium constants which in turn depend on the assumed bonding configurations (usually monodentate or bidentate). Finally, the distribution of specific types of sites and surface defect structures can be considerably different between powders and single crystals of the same phase. Ultimately, precise knowledge of the distance and distribution of ions near the charged mineral–aqueous solution interface of the kind demonstrated here, coupled with parallel potentiometric titration measurements under identical solution conditions will provide a stricter test of these models (10). Such studies may help to constrain these modeling efforts more tightly and to determine whether new modeling

approaches might ultimately be necessary to fully utilize the molecular-level detail that *in situ* structural probes, such as the Bragg XSW technique, provide (1).

For instance, the condensed layer capacitance for Sr ion adsorption on rutile had previously been derived on the basis of a bidentate adsorption geometry (18). However, the present results instead imply a tetradentate adsorption geometry. While such inconsistencies are implicit in the comparisons described above, they must ultimately be reconciled before the nominal agreement between these two approaches can be considered to be significant. To demonstrate the ultimate value of a detailed comparison of potentiometric titration and XSW measurements, we will for the sake of argument assume that this geometric inconsistency does not change the results substantially. Since the capacitances derived based on the XSW measurements had assumed a bulk dielectric constant of  $\epsilon_b = 78.5$ , the discrepancy between the two sets of derived capacitances can be resolved simply by assuming a near-surface dielectric constant of  $\sim 40$ . This reduction in the dielectric constant suggests that the near surface water is polarized as expected for a highly charged interface (1). Therefore the coupling of these two complementary techniques provides, in principle, a new and powerful method of probing the polarization of near-surface water.

#### *In Situ Measurements of EDL Partitioning*

An important result of the Bragg XSW measurements is that they also provide a direct measure of the partitioning of ions between the condensed and diffuse layers. The data in Fig. 7 were taken in a pH range where the rutile (110) surface is negatively charged, and consequently cations will be attracted to the rutile surface. Indeed, the data show a well-defined coherent position for both Sr and Rb ions. As will be shown below, the  $f$  value of the diffuse layer is negligible whenever its characteristic length scale (i.e., the Debye length) of that distribution is large compared with the period of the X-ray standing wave (in this case, 3.25 Å). Therefore, the significant (i.e., nonzero) value of the measured  $f$  value immediately implies that a significant fraction of the Sr and Rb ions are located in well-defined adsorption sites at the rutile (110)–water interface. That is, a significant fraction of these ions must populate the condensed layer under these *in situ* conditions.

An important feature of these data is that the  $f$  value is found to systematically increase with the cation solution concentration (Fig. 10). Previous *in situ* XSW measurements of ion adsorption from solution have typically observed that the measured coherent fraction often decreases as the solution concentration increases. This may occur either as a simple dilution of the XSW signal by fluorescence from ions in the bulk solution layer (see below for more detail) (35), or through the enhanced formation of ion-containing surface precipitates (36). Because we observe that the coherent fraction increases with ion concentration, we can rule out these two phenomena. To understand this observation, we note that the measured coherent fraction,  $f$ , can be generally written as the product of a Debye–Waller factor to

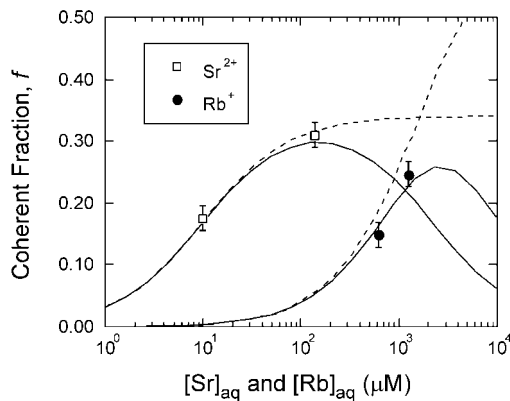


**FIG. 10.** Variation of  $f$  values for Sr and Rb as a function of aqueous concentration. The solid and dashed lines show the behavior of the measured coherent fraction with and without, respectively, the influence of the projected bulk solution coverage,  $\Theta_{\text{bulk}}$ . This highlights the reduction in the predicted coherent fraction at high concentrations ( $>1000 \mu\text{M}$ ) due solely to the dilution of the XSW signal due to the bulk solution concentration, as described in Eq. [5]. The calculations for the Sr data use values of  $K_{\text{ads}} = 0.08 \mu\text{M}^{-1}$  and  $X_{\text{max}} = 0.36$ , and assume an EDL coverage of 0.5 ML and a solution thickness of  $2 \mu\text{m}$ . The Rb calculations use values of  $K_{\text{ads}} = 0.00063 \mu\text{M}^{-1}$ ,  $X_{\text{max}} = 0.68$ , and an EDL coverage of 1.0 ML.

account for thermal vibrations,  $D_H$ , and the geometrical factor,  $a_H$ , that describes the adsorbate structure, or

$$f = D_H a_H. \quad [3]$$

The Debye–Waller factor approaches unity for chemisorbed species at room temperature when  $H$  is a low-order reflection (37). The geometrical factor of the EDL,  $a_H$ , can be calculated as the magnitude of the Fourier transform of the ion density distribution function and therefore depends on the detailed adsorption structure of the ion. For the simple case of ions adsorbed at a unique site,  $a_H = 1$ . The value of  $a_H$  diminishes for multiple site adsorption. As an extreme example,  $a_H = 0$  for the case of two equally occupied sites that are displaced by  $d_H/2$  (this case being analogous to the structure factor being zero for a forbidden Bragg peak).

In the present measurements, the  $f$  value for the (110) reflection can be calculated as the average of the geometrical factors,  $a_{110}$ , of the condensed, diffuse, and bulk layers weighted by their respective two-dimensional coverages (i.e., projected onto the surface plane). The geometrical factor of the bulk solution layer is by definition equal to zero. If we assume a diffuse ion distribution that is characterized by an exponential decay, ions in the diffuse layer appear to the Bragg XSW technique as a random contribution to the fluorescence yield and would therefore have a geometrical factor that is essentially equal to zero. For instance, the ionic strengths used in the present measurements are  $\leq 4240 \mu\text{M}$  corresponding to Debye lengths of  $>50 \text{Å}$ . These conditions result in a geometrical factor of  $<0.01$  when measured with the rutile (110) Bragg peak. The ion adsorption structure in the condensed layer can be characterized by a geometrical factor,  $a_c$ . Consequently, the measured coherent

fraction for the EDL can be written as

$$f = \Theta_c a_c / (\Theta_c + \Theta_d + \Theta_{\text{bulk}}) \cong \Theta_c a_c / (\Theta_c + \Theta_d) = X a_c, \quad [4]$$

where  $\Theta_i$  is the projected coverage of the condensed (c), diffuse (d), and bulk solution layers, respectively. For a sufficiently thin film of “bulk” solution, the projected surface concentration of the bulk solution ions,  $\Theta_{\text{bulk}}$ , is negligible with respect to the projected coverage of the ions in the EDL. For instance, for  $[\text{Sr}]_{\text{aq}} < 200 \mu\text{M}$  and with a solution thickness of  $2 \mu\text{m}$ ,  $\Theta_{\text{bulk}} < 0.046 \text{ ML}$ . In this limit the measured coherent fraction is equal to the product of the fraction of double-layer ions in the condensed layer,  $X = \Theta_c / (\Theta_c + \Theta_d)$ , and the geometrical factor of the condensed layer. We can refer to  $X$  as the double-layer partition coefficient. Thus, the measured  $f$  value is directly proportional to the double-layer partition coefficient,  $X$ . (For cases where  $\Theta_{\text{bulk}}$  is significant, independent knowledge of the total projected ion coverage,  $\Theta_{\text{tot}} = \Theta_c + \Theta_d + \Theta_{\text{bulk}}$ , as well as the thickness and concentration of the bulk solution, allow  $X$  to be determined from  $f$ .)

Based on this analysis, the observed increase in  $f$  as a function of  $[\text{Sr}]_{\text{aq}}$  can be attributed to a change in either the partition coefficient,  $X$ , or the geometrical factor,  $a_c$ . From the analysis of the *ex situ* XSW data we concluded that there exists a single adsorption site over this range of conditions (or, alternatively, if there were to be more than one adsorption site that the relative populations of these sites must be fixed). This conclusion is also supported by the *in situ* data. This implies that  $a_c$  does not vary significantly as a function of ion concentration. The increase in the measured *in situ*  $f$  value with increasing  $[\text{Sr}]_{\text{aq}}$  and  $[\text{Rb}]_{\text{aq}}$  can therefore be associated with changes in the partition coefficient,  $X$ . In other words, the fraction of ions in the condensed layer increases as both  $[\text{Sr}]_{\text{aq}}$  and  $[\text{Rb}]_{\text{aq}}$  increase.

#### Detailed Analysis and Comparison of *in Situ* and *ex Situ* XSW Results

Although limited in extent, the data in Fig. 10 are sufficient to obtain order-of-magnitude estimates for the parameters that characterize the observed behavior, and to compare the partitioning behavior of Sr and Rb ions. In the regime where the solution ion concentration is negligible (i.e.,  $\Theta_{\text{bulk}} \sim 0$ ) we can use Eq. [4],  $f = X a_c$ , and the primary uncertainty in deriving  $X$  from  $f$  is associated with the value to the geometrical factor of the condensed layer,  $a_c$ . From the *ex situ* Sr XSW measurements, we know that  $f$  can be as large as 0.63, and from the discussion above we concluded that  $a_c$  does not vary as a function of the solution ion concentration. Since  $f = X a_c$  (when  $\Theta_{\text{bulk}}$  is negligible) and  $X \leq 1$ , we can infer from the *ex situ* data that  $0.63 < a_c < 1.0$ . While further measurements can uniquely define  $a_c$ , we initially assume that  $a_c \sim 1$ .

To compare the Sr and Rb data in Fig. 10, we assume that the variation of individual parameters ( $\Theta$ ,  $X$ , ...) can be modeled using the form of a Langmuir adsorption isotherm, e.g.,  $X([\text{Sr}]_{\text{aq}}) = X_{\text{max}}/[1 + 1/(K_{\text{ads}}[\text{Sr}]_{\text{aq}})]$ . Here  $X_{\text{max}}$  repre-

sents the maximum partition coefficient and  $K_{\text{ads}}$  is identified as the equilibration constant corresponding to the surface adsorption reaction  $[\text{A}] + [\text{S}] \rightleftharpoons [\text{AS}]$ , where  $K_{\text{ads}} = [\text{AS}]/[\text{A}]_{\text{aq}}[\text{S}]$ . Here  $[\text{A}]_{\text{aq}}$  is the solution concentration of the ion,  $[\text{S}]$  is the site density, and  $[\text{AS}]$  is the surface adsorbate density which in appropriate units is equal to the surface coverage,  $\Theta$ .  $K_{\text{ads}}$  therefore has units of  $\mu\text{M}^{-1}$ . We have so far ignored the influence of the ion concentration in the bulk solution. Its influence on the measured coherent fraction can be derived from Eq. [4] as

$$f = \Theta_c a_c / (\Theta_c + \Theta_d + \Theta_{\text{bulk}}) \\ = X([\text{Sr}]_{\text{aq}}) a_c [1 + (\Theta_{\text{bulk}}/(\Theta_c + \Theta_d))]^{-1}. \quad [5]$$

It is only in the last term of this expression,  $[1 + (\Theta_{\text{bulk}}/(\Theta_c + \Theta_d))]^{-1}$ , that the influence of the bulk solution ion concentration is found. For instance, with a solution thickness of  $2 \mu\text{m}$  and an EDL coverage of 0.5 ML, this term would reduce the measured coherent fraction by 5% at  $[\text{Sr}]_{\text{aq}} = 100 \mu\text{M}$  and 50% at  $[\text{Sr}]_{\text{aq}} = 1000 \mu\text{M}$ . Therefore the derivation of  $X$  from  $f$  requires the additional independent knowledge of the ratio of the surface charge density (which we assume is equal in magnitude to the sum of  $\Theta_c + \Theta_d$ ) and the solution thickness (which determines  $\Theta_{\text{bulk}}$  for a given solution concentration) at high ion concentrations.

To demonstrate the influence of bulk ion concentration on the interpretation of the data, we show two sets of curves in Fig. 10. In each case, the dashed line ignores the influence of the bulk solution ion concentration while the solid line includes it according to Eq. [5]. We assume that the rutile surface charge is the same for the Rb and Sr measurements and consequently that the total EDL coverage of  $\text{Rb}^+$  (for both condensed and diffuse layers) will be twice that of the  $\text{Sr}^{2+}$ . The difference between the solid and dashed curves for each set of data clearly demonstrates the importance of properly including the bulk ion concentration, especially at high solution concentrations.

Using Eq. [5] and allowing the ratio of the solution thickness to EDL coverage to vary arbitrarily (since these parameters are not directly measured), we find that the Sr data are characterized by the parameters  $X_{\text{max}} = 0.40 \pm 0.08$  and  $K_{\text{ads}} = 0.12 \pm 0.08 \mu\text{M}^{-1}$ . [We have so far arbitrarily assumed that  $a_c = 1$ . If we set the condensed layer geometrical factor to be the minimum value consistent with the data,  $a_c = 0.63$ , we find that  $X_{\text{max}} (\textit{in situ}) = 0.63 \pm 0.13$  (this assumption has no influence on the derived equilibrium constant,  $K_{\text{ads}}$ ).]

To test the validity of these results, we can independently estimate these parameters from the *ex situ* XSW measurements. The *ex situ* Sr coherent coverage,  $\Theta_{\text{coh}} = \Theta_{\text{tot}} f$  (where  $\Theta_{\text{tot}}$  is the measured *ex situ* coverage), is characterized by the relation,  $\Theta_{\text{coh}}(\text{ML}) = 0.37/(1 + 13.6/[\text{Sr}]_{\text{aq}})$ , where the numerical values in this expression are found by fitting to the data in Fig. 4. We take this as an estimate for the *in situ* condensed layer coverage. A lower limit on the total EDL Sr coverage is the maximum measured *ex situ* coverage (0.54 ML as seen in Fig. 4) because (1) some Sr ions in the diffuse layer will probably fail to adsorb

to the surface during the removal of the sample from solution so that the measured coverage will be less than the total EDL coverage, and (2) we know from the *ex situ* coverage measurement at pH 3.2 that there is insignificant nonspecific adsorption from the “bulk” solution under our conditions. With this reasoning we can estimate the partition coefficient derived from the *ex situ* data as  $X([\text{Sr}]_{\text{aq}}) = \Theta_{\text{coh}}/0.54 \text{ ML} = X_{\text{max}}/(1 + 1/(K_{\text{ads}} [\text{Sr}]_{\text{aq}}))$ , where  $X_{\text{max}}(\textit{ex situ}) < 0.69$  and  $K_{\text{ads}} = 0.074 \mu\text{M}^{-1}$ . Therefore the *in situ* and *ex situ* data provide consistent results in terms of the EDL partitioning, characterized by  $X_{\text{max}}$  and  $K_{\text{ads}}$ . This consistency between the *in situ* and *ex situ* results implies (1) that the understanding that we derive through the XSW measurements is representative of the intrinsic EDL structure, and (2) that the *ex situ* data provide useful information about the *in situ* ion partitioning (at least in this particular case).

Taking together all of the uncertainties in the maximum partitioning coefficient discussed above we find that  $X_{\text{max}} = 0.5 \pm 0.25$ . While not very precise, this result clearly demonstrates that the partitioning of the Sr ions between the condensed and diffuse layers saturates at a value that is substantially smaller than 1.0. In other words  $\text{Sr}^{2+}$  is portioned more or less equally between the condensed and diffuse layers under our experimental conditions at the highest Sr ion concentrations. We expect to document significant changes in this distribution in future experiments in which ionic strength and composition as well as pH are varied over a wider range of conditions. In any case, this represents the first direct *in situ* measurement of ionic distribution across the entire double-layer region of which we are aware.

In a similar way, we can also quantify the partitioning behavior of Rb ions. Our results reveal that the partitioning of  $\text{Rb}^+$  ions is described by  $X_{\text{max}}(\textit{in situ}) = 0.7 \pm 0.3$  and  $K_{\text{ads}} = 0.0008 \pm 0.0005 \mu\text{M}^{-1}$ . These parameters are less precise than those for Sr, because they were taken with high solution concentrations in a regime where they are more directly sensitive to the specific solution thickness (which was not independently measured). However, these results clearly show that the value of  $K_{\text{ads}}$  for  $\text{Rb}^+$  is  $\sim 150$  times smaller than that of  $\text{Sr}^{2+}$  and imply that, all else being equal, the Sr–rutile interaction is substantially stronger than the Rb–rutile interaction. These results are also consistent with recent results for  $\text{Ca}^{2+}$  and  $\text{Na}^+$  ions (6, 19) that provide estimates of the equilibrium constant,  $K_{\text{ads}}$ , as inferred from potentiometric titration data (6, 19). These studies reveal that the ratio of equilibrium constants for Ca and Na is  $\sim 300$ . However, these models do not uniquely define these equilibrium constants because of their inverse covariance with associated capacitance terms (which are proportional to ion height as noted above) in the double-layer models. Despite this weaker interaction strength, the maximum  $\text{Rb}^+$  ion partitioning coefficient,  $X_{\text{max}}$ , is found to be comparable to that of the  $\text{Sr}^{2+}$  ion. We note, however, that the difference in pH between the Sr and Rb experiments (10.6–10.9 vs 7.9–9.9, Fig. 4) and the ionic strength differences noted above are likely to influence these comparisons. For instance, the lower pH of the

Rb measurements is expected to reduce (at any given solution concentration) ion partitioning into the condensed layer [e.g., Ref. (19)]. Future experiments will more carefully control and more systematically vary pH and ionic strength to determine the precise influence of these variables on EDL structure. Ultimately, the ability of XSW techniques to determine both ion height and  $K_{\text{ads}}$  values will uniquely constrain applicable EDL models.

## SUMMARY

We have demonstrated the capability to directly probe important aspects of the EDL at mineral–fluid interfaces by using the Bragg XSW technique in both *in situ* and *ex situ* measurements and *ex situ* SEXAFS measurements. Aspects of the EDL structure that can be directly probed in this manner include the location of ions in the condensed layer and the partitioning of ions between the condensed and diffuse layers as a function of pH and solution ion concentration. The comparison of SEXAFS and XSW results for Sr provides a detailed picture of the condensed layer ion structure. Through comparison of *in situ* and *ex situ* measurements, we find consistent results concerning the maximum double-layer partition coefficient,  $X_{\text{max}}$ , and the ion–substrate equilibrium constant,  $K_{\text{ads}}$ . We have also measured the differences in the condensed layer locations and the relative strength of the ion–substrate interaction for Rb and Sr ions. Substantially higher precision measurements of the EDL can be anticipated in future measurements when coupled with additional measurements of such features as the condensed layer geometrical factor, the total EDL coverage, and the solution thickness. These results suggest that these aspects of the ion distribution near a mineral–water interface can now be measured directly, *in situ*, to yield a truly atomistic understanding of the EDL structure.

## APPENDIX: NOMENCLATURE

---

$a_H$	Geometrical factor of the EDL for an arbitrary Bragg reflection, where $H = hkl$ denotes the Bragg condition
$a_c$	Geometrical factor of the condensed layer
$D_H$	Debye–Waller factor for the Bragg reflection, $H = hkl$
$f$	Coherent fraction
$K_{\text{ads}}$	Equilibrium constant for the ion adsorption reaction $A + S \rightleftharpoons AS$ , defined as $K_{\text{ads}} = [\text{AS}]/[\text{A}]_{\text{aq}}[\text{S}]$ , where $[\text{A}]_{\text{aq}}$ is the solution concentration of the ion, $[\text{S}]$ is the site density, and $[\text{AS}]$ is the surface adsorbate density
ML	Monolayer, a unit of surface coverage; 1 ML = 1 ion/19.24 Å <sup>2</sup> for a TiO <sub>2</sub> (110) surface
$P$	Coherent position in units of the substrate $d$ spacing (here, $d_{110} = 3.25$ Å)

$R(\theta)$	X-Ray reflectivity, measured as a function of the incident angle, $\theta$
SEXAFS	Surface extended X-ray absorption fine structure
$\Theta_i$	Surface coverage in units of ML, where $i$ denotes the condensed layer (c), the diffuse layer (d), or the two-dimensional projected bulk solution coverage (bulk). For <i>ex situ</i> measurements, $i$ denotes the total (tot) and coherent (coh) coverages, the latter defined as $\Theta_{\text{coh}} = \Theta_{\text{tot}} f$ , where $f$ is the coherent fraction
$\theta_B$	Bragg angle as determined from Bragg's law (i.e., in the absence of refractive and dynamical effects) measured with respect to the surface plane
$X$	Double-layer partition coefficient, $X = \Theta_c / (\Theta_c + \Theta_d)$
XSW	X-Ray standing waves
$Y_{\text{OB}}$	Off-Bragg fluorescent yield (i.e., in the absence of a Bragg reflected X-ray beam)
$Y_{\text{Sr}}(\theta)$	Fluorescent yield (e.g., for Sr) measured as a function of the incident angle, $\theta$

### ACKNOWLEDGMENTS

The XSW experiments were performed at the undulator beamline station 12-ID-D (BESSRC-CAT) at the Advanced Photon Source at Argonne National Laboratory. The SEXAFS measurements were performed at beamline X-15A at the National Synchrotron Light Source at Brookhaven National Laboratory. The work was supported by the Geosciences Research Program, Office of Basic Energy Sciences, U.S. Department of Energy. Use of the Advanced Photon Source was supported by the Office of Basic Energy Sciences, Office of Science, U.S. Department of Energy, under Contract W-31-109-ENG-38 at Argonne National Laboratory. Use of the National Synchrotron Light Source was supported by U.S. Department of Energy under Contract DE-AC02-98CH10886. M.M. acknowledges the support of the Illinois State Water Survey and the Illinois Department of Natural Resources. We thank Phillip Geissbühler for help during the initial phase of these measurements, Dimitri Sverjensky for a careful reading of an early version of the manuscript, and David Wesolowski and three anonymous reviewers for providing constructive review comments.

### REFERENCES

- Brown, G. E., Jr., Heinrich, V. E., Casey, W. H., Clark, D. L., Eggleston, C., Felmy, A., Goodman, D. W., Gratzel, M., Maciel, G., McCarthy, M. I., Nealon, K. H., Sverjensky, D. A., Toney, M. F., and Zachara, J. M., *Chem. Rev.* **99**, 77 (1999).
- Roeder, R. K., and Slamovich, E. B., in "Aqueous Chemistry and Geochemistry of Oxides, Oxyhydroxides and Related Materials" (J. A. Voigt, T. E. Wood, B. C. Bunker, W. H. Casey, and L. J. Crosse, Eds.). Materials Research Society, Warrendale, PA, 1996.
- Stumm, W., "Chemistry of the Solid-Water Interface." Wiley-Interscience, New York, 1992.
- Dzombak, D. A., and Morel, F. M. M., "Surface Complexation Modeling: Hydrous Ferric Oxide." Wiley-Interscience, New York, 1990.
- Westall, J., and Hohl, H., *Adv. Colloid Interface Sci.* **12**, 265 (1980).
- Machesky, M. L., Wesolowski, D. J., Palmer, D. A., and Ichiro-Hayashi, K., *J. Colloid Interface Sci.* **200**, 298 (1998).
- Hiemstra, T., and van Riemsdijk, W. H., *J. Colloid Interface Sci.* **179**, 488 (1996).
- Ocko, B. M., Wang, J. X., and Wandlowski, T., *Phys. Rev. Lett.* **79**, 1511 (1997).
- Toney, M. F., and McBreen, J., *Electrochem. Soc. Interface* **2**, 22 (1993).
- Towle, S. N., Brown, G. E., Jr., and Parks, G. A., *J. Colloid Interface Sci.* **217**, 299 (1999).
- Towle, S. N., Bargar, J. R., Brown, G. E., Jr., and Parks, G. A., *J. Colloid Interface Sci.* **217**, 312 (1999).
- Wu, C. F., Chen, S. H., Shih, L. B., and Lin, J. S., *Phys. Rev. Lett.* **61**, 645 (1988).
- Sumaru, K., Matsuoka, H., and Yamaoka, H., and Wignall, G.D., *Phys. Rev. E* **53**, 1744 (1996).
- Bedzyk, M. J., Bommarito, G. M., Caffrey, M., and Penner, T. L., *Science* **248**, 52 (1990).
- Machesky, M. L., Palmer, D. L., and Wesolowski, D. J., *Geochim. Cosmochim. Acta* **58**, 5627 (1994).
- Charlton, G., Howes, P. B., Nicklin, C. L., Steadman, P., Taylor, J. S. G., Muryn, C. A., Harte, S. P., Mercer, J., McGrath, R., Norman, D., Turner, T. S., and Thornton, G., *Phys. Rev. Lett.* **78**, 495 (1997).
- Yates, D. E., and Healy, T. W., *J. Chem. Soc. Faraday Trans. 1* **76**, 9 (1980).
- Jang, H. Y., and Fuerstenau, D. W., *Colloids Surf.* **21**, 235 (1986).
- Ridley, M. K., Machesky, M. L., Wesolowski, D. J., and Palmer, D. A., *Geochim. Cosmochim. Acta* **63**, 3087 (1999).
- Jones, P., and Hockey, J. A., *Trans. Faraday Soc.* **67**, 2679 (1971).
- Koretsky, C. M., Sverjensky, D. A., and Sahai, N., *Am. J. Sci.* **298**, 349 (1998).
- Larson, I., Drummond, C. J., Chan, D. Y. C., and Grieser, F. W., *J. Am. Chem. Soc.* **115**, 11885 (1993).
- Hu, K., Fan, F.-R. F., Bard, A. J., and Hillier, A. C., *J. Phys. Chem. B* **101**, 8298 (1997).
- Berube, Y. G., and De Bruyn, P. L., *J. Colloid Interface Sci.* **27**, 305 (1968).
- Fokkink, L. G. J., De Keizer, A., and Lyklema, J., *J. Colloid Interface Sci.* **127**, 116 (1989).
- Bethke, C. M., "Geochemical Reaction Modeling: Concepts and Applications." Oxford Univ. Press, New York, 1996.
- See review by: Zegenhagen, J., *Surf. Sci. Rep.* **18**, 199 (1993), and references therein.
- Batterman, B. W., *Phys. Rev. Lett.* **22**, 703 (1969).
- Matsushita T., and Hashizume, H., "Handbook on Synchrotron Radiation," (E. Koch, Ed.), Vol. 1. North-Holland, Amsterdam, 1983.
- Stohr J., in "X-Ray Absorption: Principles, Applications, Techniques of EXAFS, SEXAFS and XANES" (D. C. Koningsberger and R. Prins, Eds.). Wiley, New York, 1988.
- Bouldin, C., Furenlid L., and Elam, T., *Physica B* **208/209**, 190 (1995).
- Sayers, D. E., and Bunker, B. A., in "X-Ray Absorption: Principles, Applications, Techniques of EXAFS, SEXAFS and XANES" (D. C. Koningsberger and R. Prins, Eds.). Wiley, New York, 1988.
- Hasnain, S. S., (Ed.), "X-ray Absorption Fine Structure." E. Horwood, New York, 1991.
- Marcus, Y., "Ion Properties. Marcel Dekker, New York, 1997.
- Sturchio, N. C., Chiarello, R. P., Cheng, L., Lyman, P. F., Bedzyk, M. J., Qian, Y., You, H., Yee, D., Geissbuhler, P., Sorensen, L. B., Liang, Y., and Baer, D. R., *Geochim. Cosmochim. Acta* **61**, 251 (1997).
- Cheng, L., *et al.*, unpublished data (1999).
- Bedzyk, M. J., and Materlik, G., *Phys. Rev. B* **31**, 4110 (1985).
- Stumm, W., "Chemistry of the Solid-Water Interface." Wiley, New York, 1992.